

A BLACK HOLE MASS DETERMINATION FOR THE COMPACT GALAXY MRK 1216

JONELLE L. WALSH¹, REMCO C. E. VAN DEN BOSCH², KARL GEBHARDT³, AKIN YILDIRIM^{2,4}, KAYHAN GÜLTEKIN⁵, BERND HUSEMANN^{2,6}, AND DOUGLAS O. RICHSTONE⁵¹ George P. and Cynthia Woods Mitchell Institute for Fundamental Physics and Astronomy, Department of Physics and Astronomy, Texas A&M University, 4242 TAMU, College Station, TX 77843, USA; walsh@physics.tamu.edu² Max-Planck-Institut für Astronomie, Königstuhl 17, D-69117 Heidelberg, Germany³ Department of Astronomy, The University of Texas at Austin, 2515 Speedway, Stop C1400, Austin, TX 78712, USA⁴ Max-Planck-Institut für Astrophysik, Karl-Schwarzschild-Str. 1, 85741 Garching, Germany⁵ Department of Astronomy, University of Michigan, 1085 S. University Ave., Ann Arbor, MI 48109, USA⁶ European Southern Observatory, Karl-Schwarzschild-Str. 2, 85748 Garching, Germany

Draft version December 8, 2016

ABSTRACT

Mrk 1216 is a nearby, early-type galaxy with a small effective radius of 2.8 kpc and a large stellar velocity dispersion of 308 km s^{-1} for its K -band luminosity of $1.4 \times 10^{11} L_{\odot}$. Using integral-field spectroscopy assisted by adaptive optics from Gemini North, we measure spatially resolved stellar kinematics within ~ 450 pc of the galaxy nucleus. The galaxy exhibits regular rotation with velocities of $\pm 180 \text{ km s}^{-1}$ and a sharply peaked velocity dispersion profile that reaches 425 km s^{-1} at the center. We fit axisymmetric, orbit-based dynamical models to the combination of these high angular resolution kinematics, large-scale kinematics extending to roughly three effective radii, and *Hubble Space Telescope* imaging, resulting in a constraint of the mass of the central black hole in Mrk 1216. After exploring several possible sources of systematics that commonly affect stellar-dynamical black hole mass measurements, we find a black hole mass of $M_{\text{BH}} = (4.9 \pm 1.7) \times 10^9 M_{\odot}$ and a H -band stellar mass-to-light ratio of $\Upsilon_H = 1.3 \pm 0.4 \Upsilon_{\odot}$ (1σ uncertainties). Mrk 1216 is consistent with the local black hole mass – stellar velocity dispersion relation, but is a factor of $\sim 5 - 10$ larger than expectations from the black hole mass – bulge luminosity and black hole mass – bulge mass correlations when conservatively using the galaxy’s total luminosity or stellar mass. This behavior is quite similar to the extensively studied compact galaxy NGC 1277. Resembling the $z \sim 2$ quiescent galaxies, Mrk 1216 may be a passively evolved descendant, and perhaps reflects a previous era when galaxies contained over-massive black holes relative to their bulge luminosities/masses, and the growth of host galaxies had yet to catch up.

Subject headings: galaxies: elliptical and lenticular, cD – galaxies: individual (Mrk 1216) – galaxies: kinematics and dynamics – galaxies: nuclei – black hole physics

1. INTRODUCTION

Our understanding of the connection between super-massive black holes and their host galaxies is anchored by ~ 100 dynamical black hole mass (M_{BH}) measurements that have been made over the past two decades (e.g., Kormendy & Ho 2013; van den Bosch 2016, and references therein). Strong correlations have emerged between M_{BH} and large-scale galaxy properties, like the bulge luminosity (L_{bul} ; e.g., Kormendy & Richstone 1995; Marconi & Hunt 2003; Kormendy & Ho 2013) or mass (M_{bul} ; e.g., Häring & Rix 2004; Sani et al. 2011; McConnell & Ma 2013), and the stellar velocity dispersion (σ_* ; e.g., Ferrarese & Merritt 2000; Gebhardt et al. 2000; Gültekin et al. 2009). These relations are connected to each other, and the search for the most fundamental one is still ongoing (Beifiori et al. 2012; Saglia et al. 2016; van den Bosch 2016). The empirical relationships imply that black holes are key components of galaxies and regulate galaxy properties via feedback mechanisms (Silk & Rees 1998; Fabian 1999), although a non-causal origin in which black holes do not actively shape their host galaxies is also possible (Peng 2007; Jahnke & Macciò 2011). Establishing the exact role of black holes in galaxy evolution and accurately inferring the black hole mass function requires increasing the num-

ber of M_{BH} measurements, specifically targeting galaxies with diverse properties that have experienced varied growth channels.

As we begin to examine a broader range of black hole masses and hosts, galaxies with different structural properties show surprises in the scaling relations. Recent progress detecting high-mass black holes in Brightest Cluster Galaxies (BCGs) and other large early-type galaxies hint that these objects may be positive outliers from $M_{\text{BH}} - \sigma_*$ and $M_{\text{BH}} - L_{\text{bul}}$ (e.g., McConnell et al. 2012; Rusli et al. 2013; Thomas et al. 2016), but there are still too few measurements to firmly characterize the scaling relations at $M_{\text{BH}} \gtrsim 10^9 M_{\odot}$. The uncertainties are equally severe at the opposite end, where spiral galaxies with low-mass black holes ($M_{\text{BH}} \lesssim 10^7 M_{\odot}$) measured from water megamaser disks exhibit substantial scatter below the global black hole – host galaxy relations (e.g., Greene et al. 2010; Läscher et al. 2016; Greene et al. 2016). There are also new observations of compact galaxies, whose black holes are a remarkably large fraction of the galaxy’s stellar mass (e.g., Seth et al. 2014; Walsh et al. 2015, 2016; Saglia et al. 2016).

NGC 1277 and NGC 1271 are two such compact galaxies, with NGC 1277 being widely studied over the last few years (e.g., van den Bosch et al. 2012; Emsellem 2013; Walsh et al. 2016; Scharwächter et al.

2016; Graham et al. 2016a). Both were originally discovered by the HET Massive Galaxy Survey (van den Bosch et al. 2015) and share considerable similarities with the $z \sim 2$ quiescent galaxies (e.g., Trujillo et al. 2014; Ferré-Mateu et al. 2015; Yıldırım et al. 2015; Yıldırım et al. 2016b, in prep). Like the $z \sim 2$ red nuggets, NGC 1277 and NGC 1271 have small effective radii of $R_e \sim 1 - 2$ kpc, stellar masses of $M_\star \sim 10^{11} M_\odot$, and stellar mass surface density profiles that are elevated at the center and drop off steeply at larger radii compared to low-redshift early-type galaxies. In addition, NGC 1277 and NGC 1271 are rotating, consistent with the disk-like flattened structures of the $z \sim 2$ red nuggets (van der Wel et al. 2011), and have uniformly old stellar populations (ages of ~ 10 Gyr) extending out to several R_e . The red nuggets are thought to grow in size and moderately in mass through mergers to produce the present-day massive galaxies (e.g., van Dokkum et al. 2010), with a small fraction experiencing passive evolution since $z \sim 2$ (e.g., Trujillo et al. 2009; Wellons et al. 2016). NGC 1277 and NGC 1271 appear to be such relics of the red nuggets, and could provide the unique opportunity to gain insight into the black holes at earlier epochs.

Of the current galaxies with dynamical M_{BH} measurements, NGC 1277 and NGC 1271 are most similar to NGC 4342 (Cretton & van den Bosch 1999) and NGC 1332. All are nearby galaxies that are flattened and rotating, with small effective radii and large stellar velocity dispersions for their luminosities. They contain black holes that are more massive than the predictions from $M_{\text{BH}} - L_{\text{bul}}$, yet are consistent with $M_{\text{BH}} - \sigma_\star$. The magnitude of the offset from $M_{\text{BH}} - L_{\text{bul}}$ depends on the adopted bulge luminosity (e.g., Walsh et al. 2015, 2016; Graham et al. 2016a,b), although we note that NGC 1332 may very well be consistent with the black hole relations given the uncertainties associated with both M_{BH} (Rusli et al. 2011; Barth et al. 2016a,b) and the bulge component (Rusli et al. 2011; Kormendy & Ho 2013; Savorgnan & Graham 2016; Saglia et al. 2016). Clearly, additional mass measurements of black holes in NGC 1277-like galaxies are needed. A significant sample of local analogs to the $z \sim 2$ red nuggets that are also positive outliers from $M_{\text{BH}} - L_{\text{bul}}$ would suggest that this black hole scaling relation did not apply at earlier times, galaxies instead harbored over-massive black holes, and subsequent galaxy growth had yet to occur.

Beyond the connections to the $z \sim 2$ red nuggets, the compact galaxies are interesting because they occupy the sparsely populated upper-end of the M_{BH} relationships, and their properties are quite distinct from the BCGs and giant ellipticals that are expected to house the most massive black holes in the Universe. Currently, at the high-mass end, the differing behaviors of $M_{\text{BH}} - \sigma_\star$ and $M_{\text{BH}} - L_{\text{bul}}$, and the poorly characterized scatter in M_{BH} for fixed σ_\star or L_{bul} , lead to strongly divergent predictions of the black hole mass function (Lauer et al. 2007a). This in turn affects inferences about black hole growth histories and constraints of the mean radiative efficiency of black hole accretion, the duty cycle of active galactic nuclei, and the redshift evolution of the scaling relations (e.g., Marconi et al. 2004; Lauer et al. 2007b; Shankar et al. 2009; Robertson et al. 2006).

In this paper, we examine Mrk 1216, an early-type,

compact ($R_e = 2.8$ kpc, $M_\star = 1.6 \times 10^{11} M_\odot$), high-dispersion ($\sigma_\star = 308 \text{ km s}^{-1}$) galaxy found through the HET Massive Galaxy Survey. Yıldırım et al. (2015) presented wide-field integral-field spectroscopy of Mrk 1216, and constructed axisymmetric Schwarzschild models in order to learn about the galaxy’s dynamical stellar mass-to-light ratio and dark matter halo. The spatial resolution, however, was insufficient to pin down the black hole mass, and Yıldırım et al. (2015) set an upper-limit of $M_{\text{BH}} < 1 \times 10^{10} M_\odot$. Here, we use Gemini North observations assisted by adaptive optics (AO) to resolve the region where the black hole dominates the gravitational potential (the black hole sphere of influence; $r_{\text{sphere}} = GM_{\text{BH}}/\sigma_\star^2$), thereby obtaining a secure stellar-dynamical M_{BH} measurement. We assume a distance of 94 Mpc to Mrk 1216. This is the same distance adopted by Yıldırım et al. (2015) and is the Virgo + Great Attractor + Shapley Supercluster Infall value (Mould et al. 2000) for $H_0 = 70.5 \text{ km s}^{-1} \text{ Mpc}^{-1}$, $\Omega_M = 0.27$ and $\Omega_\Lambda = 0.73$. At this distance, $1''$ corresponds to 456 pc.

The paper is structured as follows. We review the imaging observations and the luminous mass model in Section 2. In Sections 3 and 4, we describe the high angular resolution and the large-scale spectroscopic observations, the measured stellar kinematics, and the point-spread function (PSF) characterizations. An overview of the stellar-dynamical models and the results from those models, including an examination of the black hole mass error budget, is provided in Section 5. We study the galaxy’s orbital structure in 6, and discuss the location of Mrk 1216 on the black hole mass – host galaxy relationships, as well as the implications, in Sections 7 and 8. Concluding remarks are provided in Section 9.

2. HST IMAGING

We obtained an *HST* Wide-Field Camera 3 (WFC3) *F160W* image of Mrk 1216. The WFC3/IR observations were executed under program GO-13050, and included dithered full array images and brief subarray exposures with a total integration time of 1354 s. The data were reduced, and the flattened, calibrated images were corrected for geometric distortions, cleaned, and combined using AstroDrizzle (Gonzaga et al. 2012) to produce a super-sampled image with a scale of $0''.06 \text{ pixel}^{-1}$. After masking the foreground stars, we described the galaxy’s stellar surface brightness distribution as the sum of two-dimensional (2D) Gaussians. Such a Multi-Gaussian Expansion (MGE; Monnet et al. 1992; Emsellem et al. 1994) is able to recover the surface brightness profiles of realistic multi-component galaxies while also allowing for the intrinsic luminosity density to be determined through an analytical deprojection. During the MGE fit, we took into account the WFC3 PSF from van der Wel et al. (2012). The PSF was generated with TinyTim (Krist & Hook 2004) for the *F160W* filter and a G2 V star at the center of the WFC3 detector, then drizzled to produce the same scale as our final Mrk 1216 image.

The Mrk 1216 MGE is composed of 10 Gaussians with dispersions, measured along the major axis, of $0''.09 - 29''.76$, and projected axis ratios between 0.52 and 0.99. The components have the same center, and a position angle of 70.2° east of north. The final param-

ter values, after correction for Galactic extinction using the Schlafly & Finkbeiner (2011) WFC3 *F160W* value of 0.017 mag and assuming an *H*-band absolute solar magnitude of 3.32 (Binney & Merrifield 1998), are given in Yıldırım et al. (2015). The MGE fits the *HST* image very well within the central $\sim 40''$, and allows us to accurately infer the stellar gravitational potential. We refer the reader to Yıldırım et al. (2015) for additional details regarding the imaging observations, data reduction, and construction of the MGE model.

3. NIFS OBSERVATIONS AND MEASUREMENTS

In addition to the luminous mass model, stellar kinematics on scales comparable to the black hole sphere of influence are crucial inputs into the dynamical models. We therefore observed Mrk 1216 with the Near-infrared Integral Field Spectrometer (NIFS; McGregor et al. 2003) aided by the ALTitude conjugate Adaptive optics for the InfraRed (Herriot et al. 2000; Boccas et al. 2006) system on Gemini North. The observations were taken on 21 Dec 2013 under program GN-2013A-Q-1 in laser guide star (LGS) mode using an $R = 13.7$ mag star located $22''$ from the galaxy nucleus as the tip-tilt reference. Four blocks of consecutive Object-Sky-Object sequences with 600 s exposures were recorded. The observations were acquired with the *H* + *K* filter and the *K* grating centered on $2.2 \mu\text{m}$. We observed the tip-tilt star once during the night for an estimate of the PSF and an A0 V star for telluric correction. The normal baseline calibrations consisting of dark frames, flat fields, Argon/Xeon arc lamp exposures, and a Ronchi mask (to establish the spatial rectification) were taken as well.

We processed the NIFS data using PyRAF¹ and the Gemini data reduction package version 1.11, following the steps in the NIFS example scripts² for calibration, telluric, and science exposures. For the galaxy, the basic procedure consisted of preparing the raw images for processing within the NIFS data reduction package, subtracting sky frames from adjacent object exposures, flat fielding, removing bad pixels and cosmic rays, wavelength calibration, and spatial rectification. We corrected for telluric features using an A0 V star, whose spectrum had been divided by a blackbody with a temperature of 9480 K after interpolating over the Br γ absorption line. We then assembled data cubes having x and y spatial dimensions, each with a scale of $0''.05 \text{ pixel}^{-1}$, and a wavelength axis. We determined the spatial offsets between individual galaxy cubes by summing over the wavelength dimension and cross-correlating the images. These eight cubes, corresponding to a total of 1.3 hours on-source, were aligned and combined to produce the final Mrk 1216 data cube. We followed similar steps to reduce the NIFS observation of the PSF star.

3.1. Stellar Kinematics

From the reduced Mrk 1216 data cube, we measured the stellar kinematics as a function of spatial location. Specifically, we extracted the line-of-sight velocity distribution (LOSVD), parameterized by the first

four Gauss-Hermite moments, in 67 Voronoi spatial bins (Cappellari & Copin 2003) using the penalized pixel fitting (pPXF) code of Cappellari & Emsellem (2004). The spatial bins were chosen so that the galaxy spectra had a signal-to-noise ratio (S/N) $\gtrsim 40$, where the S/N was measured as the median flux divided by the standard deviation of the pPXF model residuals. Such a high S/N spectrum is required in order to measure the LOSVD's deviation from a Gaussian (e.g., van der Marel & Franx 1993; Bender et al. 1994).

We provided pPXF with a velocity template library composed of 12 stars (K0–M5 giant stars and two late-type supergiants), which were observed with NIFS in the *K* band. The stars are a subset of those presented in Winge et al. (2009), but we have reduced the data ourselves (Walsh et al. 2016), starting with the raw frames and their calibration files retrieved from the Gemini Science Archive. During the fit with pPXF, we corrected for slight differences in the continuum shape and equivalent width between the LOSVD-convolved template stars and the observed galaxy spectra via an additive constant and a multiplicative Legendre polynomial of degree 1. The LOSVD was largely constrained by the strong $^{12}\text{CO}(2-0)$ and $^{12}\text{CO}(3-1)$ bandheads, which were contained within the $2.26 - 2.39 \mu\text{m}$ fitting region. We masked the Ca I absorption line because our template library does not include cool dwarf stars (e.g., Krajnović et al. 2009), and further excluded a few artificial features, likely the result of imperfect sky subtraction or telluric correction. Example fits with pPXF to the observed galaxy spectra located at the nucleus, in an intermediate region, and in one of the outermost spatial bins are given in Figure 1.

After an initial fit to the galaxy spectrum in each spatial bin, we ran a Monte Carlo simulation with 100 iterations. During each realization, we generated a synthetic spectrum by taking the best-fit model and adding random Gaussian noise based upon the standard deviation of the model residuals. We re-fit the spectrum using pPXF with the penalization turned off. From the resulting distribution for each Gauss-Hermite moment, we took the mean to be the kinematic value and the standard deviation to be the 1σ uncertainty. Finally, we point-symmetrize the kinematics using the method described in van den Bosch & de Zeeuw (2010), which also removes the systematic offsets in the odd Gauss-Hermite moments.

The resulting radial velocity (V) map shows that Mrk 1216 is rotating, such that the southwest side of the galaxy is blueshifted and the northeast side is redshifted with values of $\pm 180 \text{ km s}^{-1}$. The velocity dispersion (σ) rises from 230 km s^{-1} at a projected radius of $\sim 1''$ to 425 km s^{-1} at the nucleus. The third Gauss-Hermite moment (h_3), or skewness, falls between ± 0.07 , and we observe a $h_3 - V$ anti-correlation, which is a common for rotating, axisymmetric systems (e.g., Fisher 1997). The map of the fourth Gauss-Hermite moment (h_4), or the kurtosis, has a slight peak at the nucleus to a value of 0.08. The kinematics have median errors of 15 km s^{-1} , 18 km s^{-1} , 0.04, and 0.04 for V , σ , h_3 , and h_4 , respectively. Table 1 provides the extracted Gauss-Hermite moments for each NIFS spatial bin, and the 2D velocity fields are shown in Figure 2.

¹ PyRAF is a product of the Space Telescope Science Institute, which is operated by AURA for NASA

² <http://www.gemini.edu/sciops/instruments/nifs/data-format-and-reduction>

TABLE 1
NIFS KINEMATICS

x ($''$)	y ($''$)	V (km s^{-1})	ΔV (km s^{-1})	σ (km s^{-1})	$\Delta\sigma$ (km s^{-1})	h_3 (7)	Δh_3 (8)	h_4 (9)	Δh_4 (10)
-0.055	0.003	-1.205	12.708	425.376	17.927	-0.010	0.024	0.075	0.031
0.012	-0.069	54.401	14.221	424.049	20.599	-0.023	0.028	0.082	0.034
0.013	0.079	-52.747	14.410	420.777	20.519	0.024	0.028	0.083	0.033
0.087	-0.012	17.161	13.271	415.750	18.381	-0.000	0.026	0.072	0.034
0.107	0.092	-46.839	13.620	369.604	17.681	0.031	0.027	0.063	0.033

NOTE. — The first two columns provide the x and y locations of the Voronoi bin generators, while the remaining columns present the point-symmetrized NIFS kinematics and their uncertainties. The position angle is 283.94° , defined counterclockwise from the galaxy's major axis to x . This table is available in its entirety in machine-readable form.

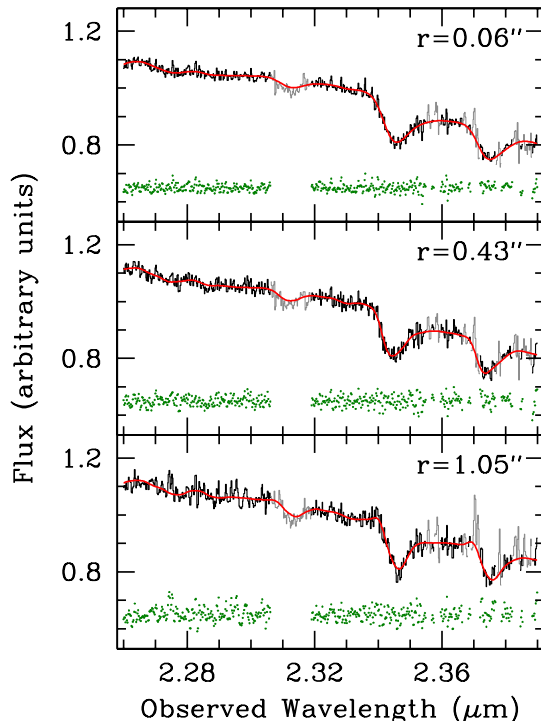


FIG. 1.— Example fits with pPXF to the observed Mrk 1216 spectra located at the nucleus (top), at an intermediate location (middle), and in one of the outermost spatial bins (bottom). The red line shows the optimal stellar template convolved with the LOSVD, whose shape is further adjusted with an additive constant and a first-degree multiplicative Legendre polynomial. Several wavelength regions shown in gray were masked during fit, including the Ca I absorption line and artifacts from imperfect data reduction. The green dots are the model residuals that have been shifted upward by a constant, arbitrary amount.

We also examined the robustness of the stellar kinematics by changing how the measurements were made with pPXF. We modified the fitting region to be longer ($2.26 - 2.43 \mu\text{m}$) and shorter ($2.26 - 2.37 \mu\text{m}$), included the Ca I absorption line in the fit, required that the relative mix of template stars remain the same between spatial bins, and tested different combinations of degree 0 – 2 multiplicative polynomials along with no additive component, an additive constant, and first-degree additive Legendre polynomial. We found the kinematics were consistent within 2σ compared to our default fitting approach. We note that there were a number of bins whose kinematics were inconsistent at the 1σ level, with the number of discrepant bins ranging from 0 – 15 depend-

ing on the fitting method being adopted. In Section 5.2, we test the effect on M_{BH} if the kinematics from an alternative fitting approach in which a multiplicative degree 2 polynomial and no additive term is used instead.

3.2. PSF Model

We described the NIFS PSF as the sum of two concentric, circular Gaussians. Following past work (e.g., Krajnović et al. 2009; Seth et al. 2014), the MGE in Section 2 was convolved with the NIFS PSF and compared to the Mrk 1216 data cube, after collapsing along the wavelength axis. This resulted in best-fit values of $0''.07$ and $0''.36$ for the dispersions, and 0.56 and 0.44 for the weights of the inner and outer Gaussian components, respectively. The method further allowed us to determine the center of the NIFS aperture. Attempts to fit a three-Gaussian PSF model produced a negligible component that contributed 1% to the total flux. Our characterization of the NIFS PSF is consistent with expectations of the Gemini ALTAIR system (e.g., Gebhardt et al. 2011; Onken et al. 2014; Drehmer et al. 2015).

We also measured the PSF using an LGS AO NIFS observation of the galaxy's tip-tilt star. With the 2D image decomposition package Galfit (Peng et al. 2010), we found that the sum of three circular Gaussians fit the collapsed NIFS data cube of the star well. The Gaussians have dispersions of $0''.07$, $0''.14$, and $0''.37$ with weights of 0.39, 0.21, and 0.40. Due to the temporal variability of the AO correction, and because the observations of the star were conducted on-axis in contrast to the off-axis observations of the galaxy, we view this second PSF determination as a rough estimate. Nevertheless, we use this result to test how sensitive the inferred M_{BH} is to the assumed PSF in Section 5.1.

4. LARGE-SCALE SPECTROSCOPY

The NIFS kinematics are complemented by large-scale spectroscopic observations that provide important constraints on the stellar mass-to-light ratio and the orbital distribution (e.g., Shapiro et al. 2006). The large-scale spectra were obtained with the Potsdam Multi Aperture Spectrograph (PMAS; Roth et al. 2005) in the Pmas fiber PAK (PPAK; Verheijen et al. 2004; Kelz et al. 2006) mode from the 3.5 m telescope at Calar Alto Observatory, and from the Marcario Low-Resolution Spectrograph (LRS; Hill et al. 1998) on the Hobby-Eberly Telescope at McDonald Observatory. Yıldırım et al. (2015) and van den Bosch et al. (2015) presented the PPAK and HET data, but we provide a brief summary below.

The PPAK integration time was 1.5 hours on-source,

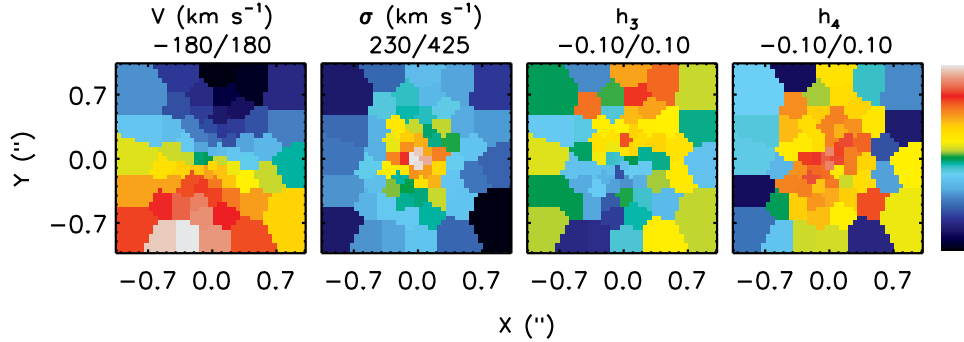


FIG. 2.— The Mrk 1216 stellar kinematics from NIFS assisted by LGS AO. The measurements are shown on the scale given by the color bar to the right, and the range of values is provided at the top of the V , σ , h_3 , and h_4 maps. Mrk 1216 exhibits regular rotation, a central rise in the stellar velocity dispersion, a $h_3 - V$ anti-correlation, and a slight peak in h_4 at the nucleus. The blueshifted velocities correspond to the southwest side of the galaxy.

with two 900 s exposures taken at three dither positions to fully sample the $331\,2''$ -wide science fibers. We acquired the data on 5 Dec 2011 with the medium resolution V1200 grating, covering $3650 - 4620\,\text{\AA}$ with a spectral resolving power of $R \sim 1650$ at $4000\,\text{\AA}$. Data reduction followed the approach of the Calar Alto Legacy Integral Field Area Survey (Sánchez et al. 2012; Husemann et al. 2013). We extracted V , σ , h_3 , and h_4 in 41 Voronoi spatial bins using pPXF, the Indo-U.S. Library of Coudé Feed Stellar Spectra (Valdes et al. 2004), and an additive Legendre polynomial of degree 15. As a final step, we point-symmetrized the stellar kinematics. The PSF was reconstructed by comparing the collapsed PPAK data cube to the Mrk 1216 MGE. The PSF has an inner Gaussian component with a dispersion of $1''.24$ that contributes 77% to the total flux, while the second Gaussian component has a weight of 23% and a dispersion of $3''.72$.

Moreover, we have a single 900 s exposure of Mrk 1216 taken with the HET/LRS $2''$ -wide slit aligned with the galaxy major axis. The g2 grating and 2×2 binning provided coverage of $4200 - 7400\,\text{\AA}$ and an instrumental dispersion of $180\,\text{km s}^{-1}$. After the initial data processing, we constructed 21 spatial bins and measured the stellar kinematics with pPXF and the MILES template library (Sánchez-Blázquez et al. 2006; Falcón-Barroso et al. 2011). Measurements of V and σ were made in each of the spatial bins, with h_3 and h_4 being extracted from the inner 10 bins. The HET data have slightly better spatial resolution than the PPAK observations, and the PSF is given by the sum of two Gaussians with dispersions of $1''.19$ and $3''.39$, each weighted by 0.55 and 0.45, respectively.

The PPAK and HET kinematics extend out to $\sim 3\,R_e$ and show features that are very similar to those seen from NIFS. The large-scale kinematics reveal that the galaxy is rotating with redshifted velocities of $\sim 160\,\text{km s}^{-1}$ to the northeast, a peak in the central velocity dispersion to $\sim 350\,\text{km s}^{-1}$, and a clear anti-correlation between h_3 and V . The PPAK and HET kinematics are consistent with the NIFS kinematics over the radial extent they share in common, after accounting for differences in spatial resolution and binning.

In order to constrain the mass of the central black hole in Mrk 1216, we calculated three-integral, orbit-based dynamical models using the triaxial Schwarzschild code of van den Bosch et al. (2008). We ran the code in the axisymmetric limit, meaning that triaxial orbit families (e.g., box orbits) are included in the orbital libraries but we adopt a nearly oblate axisymmetric shape with an intermediate to long axis ratio of 0.99. The assumption of axisymmetry is justified by the galaxy’s rotation and the absence of isophotal and kinematic twists in the *HST* image and the NIFS/PPAK data. We deprojected the MGE in Section 2 using an inclination angle of 70° . The same inclination was used by Yıldırım et al. (2015), and is mid-way between the range of angles for which the MGE can be deprojected given the apparent axis ratio of the flattest Gaussian component. Since Mrk 1216 does not contain a nuclear dust disk, we are unable to derive an independent estimate of the inclination angle, as has been possible for a few nearby galaxies (e.g., van den Bosch et al. 2012; Yıldırım et al. 2016a).

The stellar potential is combined with the gravitational potential due to a black hole and a Navarro-Frenk-White (NFW; Navarro et al. 1996) dark matter halo. We created an orbit library that samples 32 equipotential shells with logarithmically spaced radii beginning at $0''.003$, with 9 angular and 9 radial values at each energy. We ensure a smooth distribution function by bundling together 125 orbits with similar initial conditions. The 972,000 orbits were then integrated in the galaxy’s potential. We used a non-negative least squares solver to assign weights to the orbits such that the superposition matches the stellar kinematics, as well as the intrinsic and projected stellar masses to an accuracy of 1%, while accounting for PSF effects and aperture binning.

The free parameters in the model are the black hole mass, the H -band stellar mass-to-light ratio (Υ_H), the concentration (c) of the NFW halo, and the fraction of dark matter relative to the stellar mass (f_{DM}). The stellar mass-to-light ratio is assumed to be constant with radius, which is supported by the lack of color gradient in *HST* WFC3 F814W and F160W images (Yıldırım et al. 2015). We generated model grids that sampled 41 values of M_{BH} with $8.5 \leq \log(M_{\text{BH}}/M_\odot) \leq 10.5$, 28 values of Υ_H between 0.3 and $3.0\,\Upsilon_\odot$, and 24 NFW halos with $c = 5, 10, 15$ and $\log(f_{\text{DM}}) = 0.5 - 4.0$. Models without a dark halo were run as well. While the results of our fidu-

cial model grid presented in Section 5.1 were obtained by fitting to the NIFS+PPAK kinematics, in Section 5.2 we also test fitting NIFS-only and NIFS+HET kinematics. With four Gauss-Hermite moments in 108 NIFS+PPAK spatial bins, there are 432 observables. Ultimately, the best-fit model is the one with the lowest χ^2 (χ^2_{\min}), and the 1σ statistical uncertainty for a given parameter is set by marginalizing over the other free parameters and searching for where the change in χ^2 ($\Delta\chi^2 \equiv \chi^2 - \chi^2_{\min}$) is 1.0. The 3σ model fitting error is taken to be where $\Delta\chi^2 = 9.0$.

5.1. Modeling Results

We present the results of our fiducial model grid in the left panel of Figure 3, and provide a comparison between the best-fit model and NIFS/PPAK kinematics in Figure 4. We find that $M_{\text{BH}} = 4.9 \times 10^9 M_\odot$, $\Upsilon_H = 1.3 \Upsilon_\odot$, $c = 10$, and $\log(f_{\text{DM}}) = 3.5$, which translates to a halo virial mass of $5 \times 10^{14} M_\odot$. This model reproduces the observed kinematics well, and has a reduced χ^2 of 0.6. The 1σ statistical uncertainties on M_{BH} and Υ_H correspond to $(4.9^{+0.8}_{-0.7}) \times 10^9 M_\odot$ and $1.3 \pm 0.1 \Upsilon_\odot$, respectively, whereas the 3σ statistical uncertainties translate to $M_{\text{BH}} = (4.9^{+1.8}_{-1.9}) \times 10^9 M_\odot$ and $\Upsilon_H = 1.3 \pm 0.3 \Upsilon_\odot$. In contrast, the dark halo parameters are not well constrained. All three values of c are allowed within 3σ and $\log(f_{\text{DM}}) > 2.5$. Models without a dark halo are clearly ruled out, as $\chi^2_{\min} = 320$ for the models without a dark halo, which corresponds an increase of 65 relative to the best-fit model incorporating an NFW dark matter halo.

Moreover, we build into the M_{BH} and Υ_H error budgets the effect of adopting a different NIFS PSF model, using unsymmetrized kinematics, and assuming a different inclination angle. Due to the difficulties in measuring the AO PSF, it is important to test how other reasonable PSF characterizations might affect M_{BH} . Our fiducial model above utilizes a two-Gaussian description determined by comparing the galaxy’s MGE to the Mrk 1216 collapsed data cube. If instead the NIFS PSF is taken to be the sum of three concentric, circular Gaussians measured from the NIFS observation of the galaxy’s tip-tilt star, we find $M_{\text{BH}} = 5.5 \times 10^9 M_\odot$ and $\Upsilon_H = 1.3 \Upsilon_\odot$.

A similar change occurs when the observed stellar kinematics are not forced to be point-symmetric. The fiducial model was fit to NIFS and PPAK kinematics that were averaged in a two-fold manner over the major and minor axes in order to reduce noise in the kinematic measurements. When only the systematic offsets in the odd Gauss-Hermite moments are subtracted off, but no other adjustments are made, we find that $M_{\text{BH}} = 5.8 \times 10^9 M_\odot$ and $\Upsilon_H = 1.1 \Upsilon_\odot$.

In addition to fitting to the point-symmetric NIFS+PPAK kinematics, the fiducial model was run for an inclination angle of 70° . Often Schwarzschild models are calculated for a single viewing orientation, as it is computationally expensive to sample over M_{BH} , Υ_H , two dark halo parameters, and the inclination (or three angles in the case of triaxiality). In the few cases where inclination was allowed to vary, the parameter was not well constrained by the 2D line-of-sight kinematics (Krajinović et al. 2005; van den Bosch & van de Ven 2009; Walsh et al. 2012). Therefore, we determined the effect on M_{BH} and Υ_H if a near edge-on angle of 85° is

used instead. We find that M_{BH} decreases by 22% to $3.8 \times 10^9 M_\odot$ and Υ_H changes by 23% to $1.6 \Upsilon_\odot$.

By adding in quadrature the 1σ formal model fitting uncertainty and the percent change in the best-fit values relative to the fiducial model above, we ultimately find that $M_{\text{BH}} = (4.9 \pm 1.7) \times 10^9 M_\odot$ and $\Upsilon_H = 1.3 \pm 0.4 \Upsilon_\odot$ for Mrk 1216. These values are consistent with models fit to only the (bi-symmetrized) PPAK kinematics – Yıldırım et al. (2015) found a black hole mass upper-limit of $1.0 \times 10^{10} M_\odot$ and $\Upsilon_H = 1.8^{+0.5}_{-0.8} \Upsilon_\odot$, along with an NFW halo parameterized by $c = 10$ and $\log(f_{\text{DM}}) = 2.9^{+1.1}_{-2.2}$ (3σ statistical uncertainties). In addition, our dynamical H -band mass-to-light ratio is in agreement with expectations from stellar population synthesis models for both a Kroupa ($1.2 \Upsilon_\odot$) and a Salpeter ($1.7 \Upsilon_\odot$) initial mass function, assuming solar metallicity and a ~ 13 Gyr age (Vazdekis et al. 1996). Given the black hole mass of $4.9 \times 10^9 M_\odot$ and the bulge stellar velocity dispersion of 308 km s^{-1} (see Section 7), the NIFS data, with a central $0''.1$ spatial bin, have easily resolved the $0''.49$ black hole sphere of influence.

5.2. Additional Models

The PPAK data cube provides an increase in 2D spatial coverage, more spatial bins, smaller uncertainties on the extracted kinematics, and better spectral resolution than the HET long-slit spectroscopy. Thus, we use the PPAK kinematics in place of the HET kinematics when constructing the dynamical models. If instead Schwarzschild models are fit to the NIFS+HET kinematics, we recover the same results, with $M_{\text{BH}} = (4.9^{+0.8}_{-0.7}) \times 10^9 M_\odot$ and $\Upsilon_H = 1.3 \pm 0.1 \Upsilon_\odot$ (1σ).

Likewise, we don’t see significant changes in M_{BH} and Υ_H if models are constrained by only the NIFS kinematics. By fitting to the NIFS data alone, the black hole mass is less susceptible to systematic effects that commonly plague stellar-dynamical models, such as assumptions about the dark matter halo (e.g., Gebhardt & Thomas 2009; Schulze & Gebhardt 2011; Rusli et al. 2013) and the radial form of the stellar mass-to-light ratio (e.g., McConnell et al. 2013). This comes at the expense of larger M_{BH} statistical uncertainties due to the poor constraint on Υ_H . Results of fitting orbit-based models to the NIFS kinematics alone are shown in the right panel of Figure 3, and we find that $M_{\text{BH}} = (5.9^{+1.0}_{-1.7}) \times 10^9 M_\odot$ and $\Upsilon_H = 1.4^{+0.5}_{-0.2} \Upsilon_\odot$ (1σ).

Finally, the NIFS kinematics were measured using an additive constant and a degree 1 multiplicative polynomial to account for differences in continuum shape between the velocity template library and the observed galaxy spectra. We consider these NIFS kinematics robust, as changes to how pPXF is run (see Section 3.1) produce similar kinematics. However, slight adjustments to the degree of the additive/multiplicative polynomials can cause inconsistent kinematics at the 1σ level (all are consistent within 2σ). In particular, one of the largest differences is seen when running pPXF with a multiplicative degree 2 polynomial (with no additive component), which produces 11 spatial bins in which the kinematics differ by more than 1σ relative to our adopted set of NIFS kinematics. If instead we use the NIFS kinematics extracted with pPXF and a multiplicative degree 2 polynomial, we infer $M_{\text{BH}} = (3.5^{+0.4}_{-0.5}) \times 10^9 M_\odot$ and

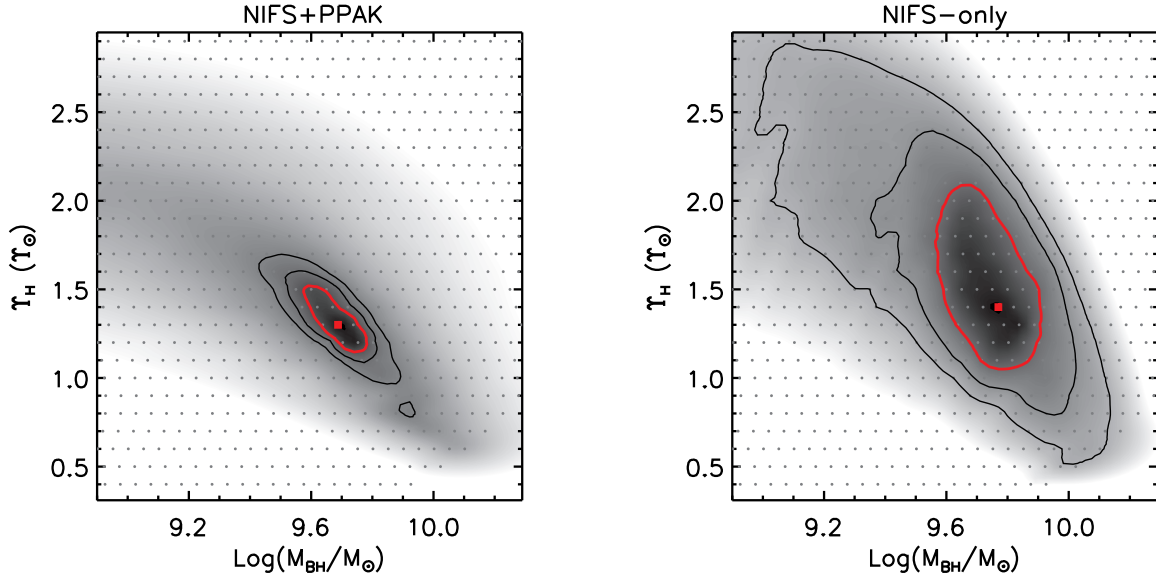


FIG. 3.— Contours of χ^2 for various stellar-dynamical models (gray dots) with different combinations of black hole mass and H -band stellar mass-to-light ratio after marginalizing over the dark halo parameters. The red square is the best-fit model, the red contour indicates where $\Delta\chi^2 = 2.3$, and the subsequent black contours correspond to $\Delta\chi^2 = 6.2$ and 11.8 , respectively. These $\Delta\chi^2$ values correspond to 1σ , 2σ , and 3σ confidence regions for two parameters. The results are shown for dynamical models fit to the combination of NIFS and PPAK data sets (left) and for models fit to only the NIFS kinematics (right). The two grids produce consistent results.

$\Upsilon_H = 1.3 \pm 0.1 \Upsilon_\odot$ (1σ). We note that this second set of NIFS kinematics show systematically smaller dispersions compared to the central PPAK kinematics, hence we perform this test as a sanity check but do not incorporate the results into our M_{BH} and Υ_H error budgets.

The results from each of the three model grids above are in agreement with our final black hole mass and mass-to-light ratio measurements for Mrk 1216 of $M_{\text{BH}} = (4.9 \pm 1.7) \times 10^9 M_\odot$ and $\Upsilon_H = 1.3 \pm 0.4 \Upsilon_\odot$.

6. THE ORBITAL STRUCTURE OF MRK 1216

Not only do the Schwarzschild models provide us with constraints on the black hole mass and the stellar mass-to-light ratio, but they also allow for an examination of the galaxy's orbital structure. Figure 5 illustrates the amount of anisotropy and the orbit type as a function of radius. Using the best-fit model from Section 5.1, we plot the ratio σ_r/σ_t , where the tangential velocity dispersion is given by $\sigma_t^2 = (\sigma_\phi^2 + \sigma_\theta^2)/2$ and (r, θ, ϕ) are spherical coordinates. In order to gain an idea of the uncertainties in σ_r/σ_t , we show all the models within $\Delta\chi^2 = 1$ from our fiducial grid, and the best-fit models from the grid searches in which we assumed a different NIFS PSF, unsymmetrized kinematics, and a near edge-on inclination angle. We find that Mrk 1216 is roughly isotropic within the black hole sphere of influence, but becomes radially anisotropic with $\sigma_r/\sigma_t \sim 1.5$ at the radial extent of the PPAK kinematics. The galaxy was modeled using a triaxial Schwarzschild code (van den Bosch et al. 2008) that was run in the axisymmetric limit. Thus, the best-fit model includes contributions from box orbits, albeit a small one, making up 10% of the orbits near the nucleus and 20% at a radius of $10''$. Instead, short-axis tube orbits dominate our best-fit model, contributing ~ 60 – 90% at all radii. Long-axis tube orbits, which are important for prolate and triaxial systems, are negligible.

7. THE BLACK HOLE – HOST GALAXY RELATIONS

Placing Mrk 1216 on the black hole–host galaxy relations further requires identifying the bulge component, and currently there is a broad range of measurements in the literature. From Galfit models of the *HST* F160W image, Yıldırım et al. (2015) find an upper limit on the H -band bulge luminosity and effective radius of $L_{H,\text{bul}} = 8.3 \times 10^{10} L_\odot$ and $R_{e,\text{bul}} = 3''.42$, and a lower limit of $L_{H,\text{bul}} = 1.5 \times 10^{10} L_\odot$ and $R_{e,\text{bul}} = 1''.34$. These numbers were derived from 2-component and 4-component 2D Sersic fits for the upper and lower limits, respectively, and correspond to a bulge-to-total ratio of $B/T = 0.69$ and 0.13 . The former characterization includes a centrally concentrated component with a Sersic index of 3.61 and a projected axis ratio of 0.56 . Since this double Sersic model produced pronounced residuals, Yıldırım et al. (2015) increased the number of Sersic functions to four to obtain a good fit to the galaxy's complex structure. Each of the four components, however, have rather low Sersic indices between 0.99 and 1.61 , which complicates a morphological classification. A dynamical decomposition using orbital weights from the Yıldırım et al. (2015) best-fit Schwarzschild model support the picture depicted by the 4-component photometric decomposition. In contrast, Savorgnan & Graham (2016) argue that Mrk 1216's bulge component has an H -band luminosity of $\sim 1.2 \times 10^{11} L_\odot$ based on a one-dimensional (1D) multi-component Sersic fit to the *HST* F160W surface brightness profile. Their fit includes an intermediate-scale disk, in addition to a nuclear exponential disk and a spheroidal component. Both Yıldırım et al. (2015) and Savorgnan & Graham (2016) find that more than one Sersic component is required to match the surface brightness despite the elliptical galaxy classification in the NASA/IPAC Extragalactic Database and Hyperleda.

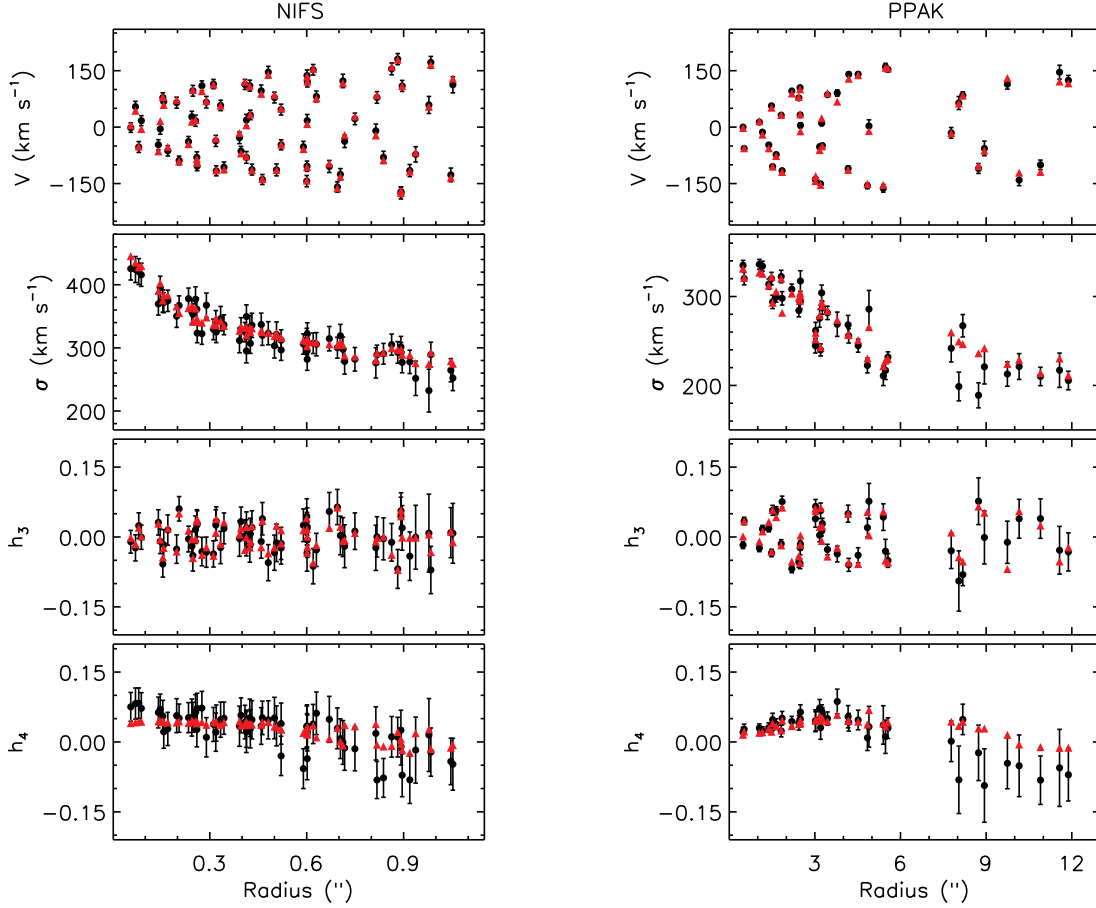


FIG. 4.— The observed NIFS (left) and PPAK (right) kinematics, plotted as a function of projected radial distance from the nucleus, are compared to the best-fit stellar dynamical model (red) with $M_{\text{BH}} = 4.9 \times 10^9 M_{\odot}$ and $\Upsilon_H = 1.3 \Upsilon_{\odot}$. The data are folded and multiple position angles are depicted. The best-fit model reproduces the kinematic features well, and has a reduced χ^2 of 0.6.

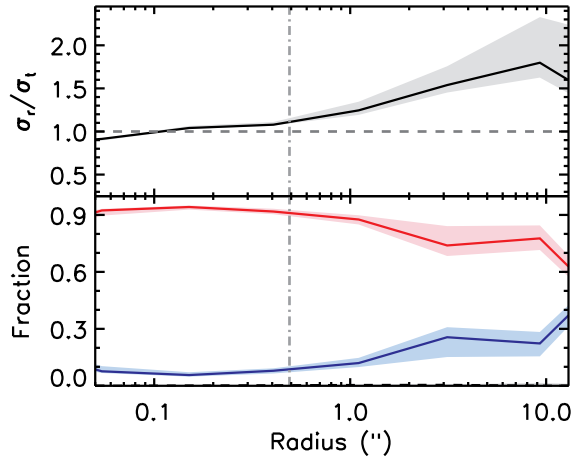


FIG. 5.— Mrk 1216’s orbital structure over the radial extent of the NIFS and PPAK kinematics. The anisotropy (top) and orbit type (bottom) are determined from the best-fit Schwarzschild model (solid lines) and a rough estimate of the uncertainties is depicted by the shaded regions. The galaxy is essentially isotropic (gray dashed horizontal line) within the black hole sphere of influence (gray dot-dashed vertical line), and becomes radially anisotropic at larger distances from the nucleus. The orbits are composed mainly of short-axis tubes (red), although a small fraction of box orbits (blue) are also present.

For Mrk 1216, we conservatively adopt limits that extend from the total quantities down to the smallest bulge measurements in the literature, with values set to the result from a 2-component 2D Sersic fit (Yıldırım et al. 2015). The galaxy’s total luminosity was determined from the MGE model in Section 2, which also agrees with a single Sersic Galfit model of the *HST* F160W image. After assuming $H - K = 0.2$ and a K -band absolute solar magnitude of 3.28 (Binney & Merrifield 1998), we establish a bulge luminosity for Mrk 1216 of $L_{K,\text{bul}} = (9.6^{+4.4}_{-7.9}) \times 10^{10} L_{\odot}$. For comparison, the upper bound on $L_{K,\text{bul}}$ derived in this manner is 36% smaller than the growth curve analysis of Two Micron All Sky Survey (Skrutskie et al. 2006) images by van den Bosch (2016). We determine the bulge mass using $\Upsilon_H = 1.3 \Upsilon_{\odot}$ from the best-fit model in Section 5.1. Although a similar compact, high-dispersion galaxy, NGC 1277, showed evidence for a radially varying V -band stellar mass-to-light ratio (e.g., Martín-Navarro et al. 2015), there is no *HST* WFC3 F814W–F160W color gradient observed for Mrk 1216 (Yıldırım et al. 2015) and a similar Υ_H from dynamical models fit to only the small-scale NIFS data in Section 5.2 and models fit to only the large-scale PPAK data (Yıldırım et al. 2015) are found. Hence, adopting $\Upsilon_H = 1.3 \Upsilon_{\odot}$ is justified and we find that $M_{\text{bul}} = (1.1^{+0.5}_{-0.9}) \times 10^{11} M_{\odot}$ for Mrk

1216. Finally, we calculate σ_* for bulge effective radii of $R_{e,\text{bul}} = 1''.34$, $3''.42$, and $6''.34$, which correspond to the measurements from a 4-component, a 2-component, and a 1-component Sersic Galfit model (Yildirim et al. 2015). We use our best-fit stellar-dynamical model to predict the luminosity-weighted second moment within a circular aperture whose radius equals $R_{e,\text{bul}}$, while also excluding the region within the black hole sphere of influence (e.g., Gebhardt et al. 2011; McConnell & Ma 2013). Thus, we determine that $\sigma_* = 308^{+16}_{-6}$ km s $^{-1}$ for Mrk 1216, which agrees well with the previous measurement of the PPAK velocity dispersion within a circular aperture that contains half of the light by Yıldırım et al. (2015).

As can be seen in Figure 6, Mrk 1216 is an outlier from the $M_{\text{BH}} - L_{K,\text{bul}}$ and $M_{\text{BH}} - M_{\text{bul}}$ relations, but is consistent with $M_{\text{BH}} - \sigma_*$. Even when using the galaxy’s total luminosity or total stellar mass, Mrk 1216 falls a factor of ~ 6 and ~ 10 above the Kormendy & Ho (2013) and Läscher et al. (2014) $M_{\text{BH}} - L_{K,\text{bul}}$ correlations, as well as a factor of $\sim 5 - 10$ above $M_{\text{BH}} - M_{\text{bul}}$ depending on whether the relation from McConnell & Ma (2013), Kormendy & Ho (2013), Savorgnan et al. (2016), Saglia et al. (2016) is assumed. Thus, using the total luminosity (stellar mass) makes Mrk 1216 a $2.2 - 2.5\sigma$ outlier ($1.4 - 3.0\sigma$ outlier) from the $M_{\text{BH}} - L_{K,\text{bul}}$ ($M_{\text{BH}} - M_{\text{bul}}$) relation given the various calibrations and scatter of the correlations. In Figure 7, we show predictions of a model with a $5.8 \times 10^8 M_\odot$ black hole, which is the mass expected from $M_{\text{BH}} - M_{\text{bul}}$ (Saglia et al. 2016) for Mrk 1216’s total stellar mass of $1.6 \times 10^{11} M_\odot$. These σ and h_4 predictions are compared to the NIFS observations and the best-fit model from Section 5.1 with $M_{\text{BH}} = 4.9 \times 10^9 M_\odot$. Our best-fit model exhibits a similar central velocity dispersion peak and elevated central h_4 values as the observed kinematics, whereas the model based on $M_{\text{BH}} - M_{\text{bul}}$ cannot reproduce these features.

For comparison, the two other compact, high-dispersion galaxies from the HET Massive Galaxy Survey are shown in Figure 6. We follow the same conventions for characterizing the NGC 1277 and NGC 1271 bulge quantities as was used for Mrk 1216. In particular, from the MGE descriptions of *HST* images (van den Bosch et al. 2012; Walsh et al. 2015) and the best-fit stellar mass-to-light ratios from dynamical models fit to AO observations (Walsh et al. 2015, 2016), we measure total luminosities of $L_V = 1.7 \times 10^{10} L_\odot$ and $L_H = 7.2 \times 10^{10} L_\odot$, and total stellar masses of $1.6 \times 10^{11} M_\odot$ and $1.0 \times 10^{11} M_\odot$ for NGC 1277 and NGC 1271, respectively. These values are similar to the total luminosities and masses reported by Emsellem (2013) for NGC 1277 and Graham et al. (2016b) for NGC 1271. Graham et al. (2016a) calculate a larger total luminosity for NGC 1277 based on modeling the 1D light profile, however their MGE model suggests a smaller total luminosity than the one adopted here (their MGE model has 43% less light than their 1D component analysis). Despite using total properties, NGC 1277 and NGC 1271 remain outliers from $M_{\text{BH}} - L_{K,\text{bul}}$ by $2.1 - 2.8\sigma$ (Kormendy & Ho 2013; Läscher et al. 2014) and $M_{\text{BH}} - M_{\text{bul}}$ by $1.4 - 3.0\sigma$ (McConnell & Ma 2013; Kormendy & Ho 2013; Savorgnan et al. 2016; Saglia et al. 2016). The two galaxies are in good agreement with the expectations

from $M_{\text{BH}} - \sigma_*$ (McConnell & Ma 2013; Kormendy & Ho 2013; Saglia et al. 2016; van den Bosch 2016).

van den Bosch (2016) conclude that $M_{\text{BH}} - \sigma_*$ is the best empirical relationship available and that a multi-variate scaling relation between M_{BH} , L_K and R_e is a projection of $M_{\text{BH}} - \sigma_*$ with an equal amount of intrinsic scatter. Previous attempts to explore whether the inclusion of an additional parameter leads to tighter scaling relations (e.g., Beifiori et al. 2012; Saglia et al. 2016) have also generally found no significant decreases in the amount of intrinsic scatter compared to the single-parameter $M_{\text{BH}} - \sigma_*$ relation. Given the arguments of van den Bosch (2016), it is not surprising that these compact galaxies are consistent with $M_{\text{BH}} - \sigma_*$ but with their small sizes are outliers from $M_{\text{BH}} - L_{\text{bul}}$. The three HET compact galaxies are in the compilation of van den Bosch (2016). With this new black hole mass and luminosities derived from the *HST* images, we find that Mrk 1216 and NGC 1271, are within $\sim 1.7\sigma$ of the black hole mass – galaxy luminosity – galaxy size relation correlation, and that NGC 1277 is consistent with the relation, given the intrinsic scatter. Future work on multi-variate scaling relations requires overcoming a sampling bias in the known M_{BH} hosts; currently there is a very limited spread in effective radii at a given K -band galaxy luminosity (van den Bosch et al. 2015).

8. DISCUSSION

Mrk 1216 hosts one of the largest black holes dynamically detected to date, naturally leading to the question of how such a massive black hole ended up in a relatively modest galaxy. One interesting explanation is that Mrk 1216 is a relic of the $z \sim 2$ quiescent galaxies, and avoided the same series of mergers that produced the typical massive early-type galaxies of today. Mrk 1216 perhaps reflects an earlier period when galaxies contained over-massive black holes for their bulge luminosities/masses, and galaxy growth had yet to follow. Such a scenario has been proposed to explain the locations of NGC 1277 and NGC 1271 on the black hole scaling relations based upon having small effective radii for the stellar masses, stellar mass surface density profiles comparable to the $z \sim 2$ red nuggets, and a uniformly old stellar population out to several R_e (e.g., Trujillo et al. 2014; Ferré-Mateu et al. 2015; Martín-Navarro et al. 2015; Yıldırım et al. 2016b, in prep). Mrk 1216 is akin to NGC 1277 and NGC 1271, and is similar to the $z \sim 2$ red nuggets. The galaxy is a clear outlier from the local galaxy mass–size relation, and has an elevated central stellar mass surface density (Yıldırım et al. 2016b, in prep). However, there are hints that Mrk 1216 has experienced some growth and begun the process of becoming a normal early-type galaxy. Mrk 1216 has one of the largest effective radii ($R_e = 2.8$ kpc) in our sample of compact galaxies found through the HET Massive Galaxy Survey, and the stellar mass surface density profile is more extended in the outer regions (Yıldırım et al. 2016b, in prep). With future work, it would be informative to study Mrk 1216’s stellar population over the extent of the galaxy.

Another possible explanation for the location of Mrk 1216 on the $M_{\text{BH}} - L_{\text{bul}}$ and $M_{\text{BH}} - M_{\text{bul}}$ relations is that we simply do not have enough measurements at the upper-end of the correlations. With the limited number of objects in this high-mass regime, nei-

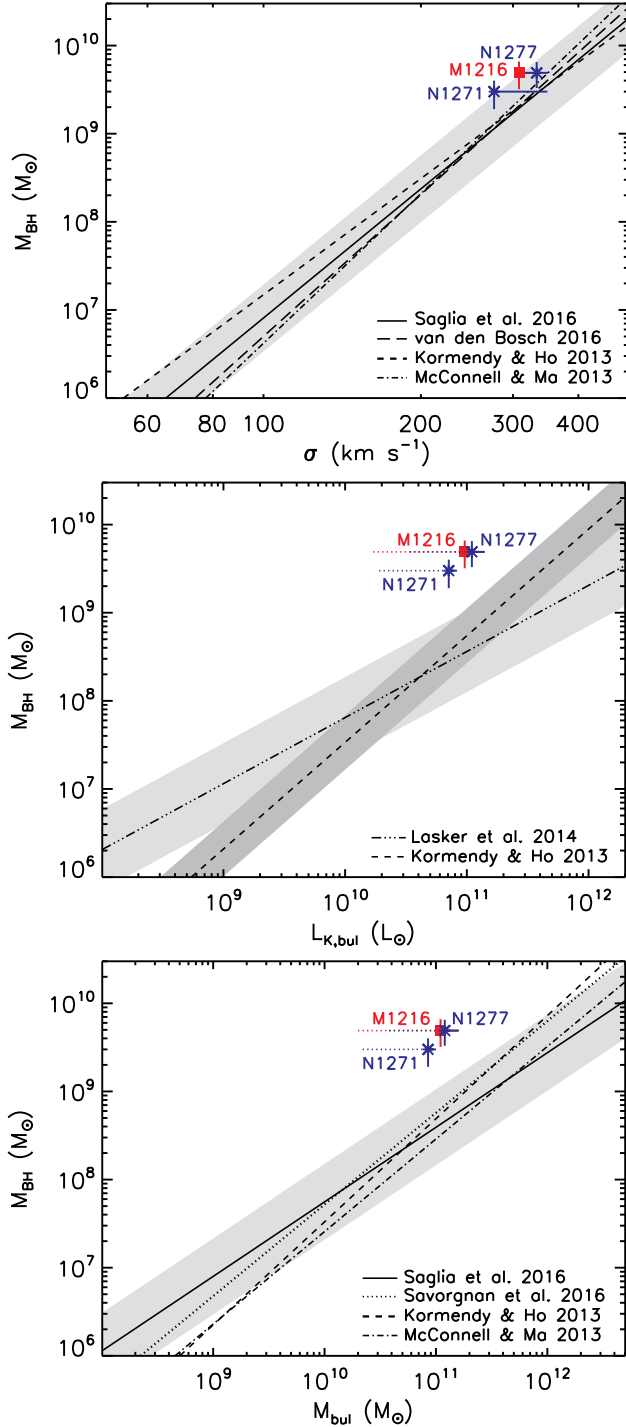


FIG. 6.— Location of Mrk 1216 (red square) on the black hole – host galaxy relations. We show multiple calibrations of the correlations, but for clarity only display the intrinsic scatter (gray) measured by Saglia et al. (2016) for the black hole mass – stellar velocity dispersion (top) and the black hole mass – bulge mass (bottom) relationships. The intrinsic scatter from both Kormendy & Ho (2013) and Lasker et al. (2014) are shown for the black hole mass – K -band bulge luminosity (middle) relationship. NGC 1277 and NGC 1271 (blue asterisks) are two compact galaxies similar to Mrk 1216 from the HET Massive Galaxy Survey with M_{BH} measurements. Due to uncertainties in the bulge components, we show limits that extend from the total quantities (upper bound of the horizontal solid line) to the smallest bulge estimates (lower bound of the horizontal dotted line) in the bottom two panels. Even when using the total luminosity/stellar mass, Mrk 1216, NGC 1277, and NGC 1271 are outliers from $M_{\text{BH}} - L_{K,\text{bul}}$ and $M_{\text{BH}} - M_{\text{bul}}$, yet are consistent with $M_{\text{BH}} - \sigma_{*}$.

ther the form of the correlations nor the magnitude and distribution of the scatter are well determined (e.g., McConnell & Ma 2013). Therefore, Mrk 1216 could fall in the tails of a distribution between black hole mass and galaxy properties that still needs to be fully flushed out. We note that many of the compact galaxies in the HET Massive Galaxy Survey have nuclear dust disks, indicating the presence of cleanly rotating gas (Ho et al. 2002; Alatalo et al. 2013), from which independent black hole mass measurements can be derived for comparison to the stellar-dynamical determinations. Such cross-checks between mass measurement methods is essential for establishing the amount of intrinsic scatter in the black hole correlations, and eventually for assessing how strongly Mrk 1216, NGC 1277, and NGC 1271 deviate from the relations. Presently, a majority of the meaningful comparisons between the stellar and gas-dynamical methods have led to discrepancies where the stellar-dynamical M_{BH} exceeds the gas-dynamical mass by factors of 2 – 3 (de Francesco et al. 2006; Rusli et al. 2011; Gebhardt et al. 2011; Walsh et al. 2012, 2013; Barth et al. 2016b), although there are a very small number of direct comparison studies.

Finally, over-massive black holes can result from tidal stripping events. This idea was used to explain the low-mass galaxy M60-UCD1, which lies a mere 6.6 kpc away from the giant elliptical galaxy M60 (Seth et al. 2014). Indeed, the EAGLE cosmological, hydrodynamical simulation (Schaye et al. 2015; Crain et al. 2015) shows that tidal stripping is the dominant process responsible for the extreme outliers from the $M_{\text{BH}} - M_{*}$ correlation, but the simulation is most sensitive to galaxies with $M_{\text{BH}} \sim 10^8 M_{\odot}$ and $M_{*} \sim 10^{10} M_{\odot}$. Due to the limited box size, predictions cannot be made for more massive NGC 1277-like galaxies (Barber et al. 2016). Contrary to NGC 1277 and NGC 1271, which are members of the Perseus cluster, Mrk 1216 is an isolated galaxy in the field, with only two other galaxies within 1 Mpc at its distance (Yıldırım et al. 2015). Combined with the regular isophotes and lack of tidal signatures in the *HST* image, the idea that Mrk 1216 was once the center of a more massive galaxy seems unlikely.

9. CONCLUSION

In summary, we measured the 2D stellar kinematics of the compact, high-dispersion galaxy Mrk 1216 using newly acquired AO NIFS observations that probe within the black hole sphere of influence. Mrk 1216 is rotating, has a distinct rise in the stellar velocity dispersion at the nucleus, exhibits the expected anti-correlation between V and h_3 , and has elevated central h_4 values. The high angular resolution NIFS kinematics, along with large-scale kinematic measurements and the luminous mass model from an *HST* image, are fit with stellar-dynamical models based upon the Schwarzschild superposition method. We constrain the mass of the central black hole in Mrk 1216 to be $(4.9 \pm 1.7) \times 10^9 M_{\odot}$ and the H -band stellar mass-to-light ratio to be $1.3 \pm 0.4 Y_{\odot}$. The error budget incorporates some possible systematic effects and the formal 1σ model fitting uncertainties.

With $\sigma_{*} = 308 \text{ km s}^{-1}$, Mrk 1216 is consistent with the $M_{\text{BH}} - \sigma_{*}$ relationship, but is a surprising positive outlier from $M_{\text{BH}} - L_{\text{bul}}$ and $M_{\text{BH}} - M_{\text{bul}}$, even when conservatively using the galaxy’s total luminosity and stellar mass

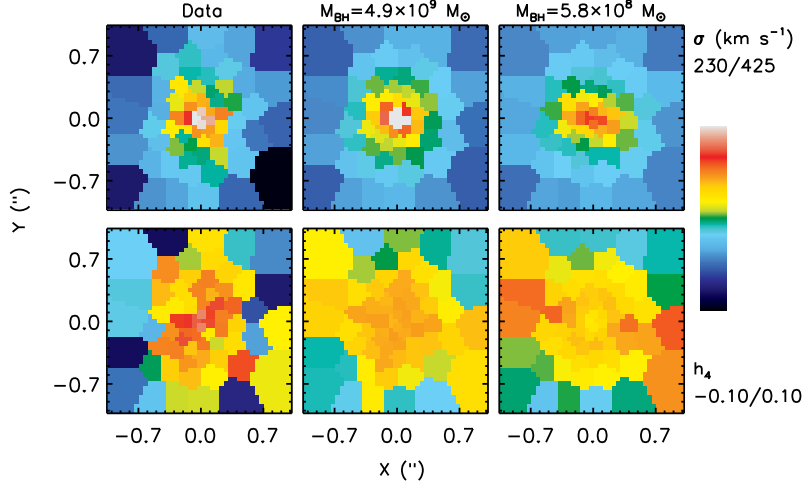


FIG. 7.— Comparison of the stellar kinematics measured from NIFS (left) to the best-fit model with a $4.9 \times 10^9 M_{\odot}$ black hole (middle) and a model with a $5.8 \times 10^8 M_{\odot}$ black hole (right), which is the mass expected from $M_{\text{BH}} - M_{\text{bul}}$ (Saglia et al. 2016) when conservatively using Mrk 1216’s total stellar mass of $1.6 \times 10^{11} M_{\odot}$. When generating models for the $5.8 \times 10^8 M_{\odot}$ black hole, we sampled over a range stellar mass-to-light ratios and dark matter halos and present the model with the lowest χ^2 . The best-fit model is a good match to the data, while the model with a smaller black hole cannot reproduce the sharp rise in the velocity dispersion (top) or the elevated h_4 values (bottom) at the nucleus.

of $L_K = 1.4 \times 10^{11} L_{\odot}$ and $M_{\star} = 1.6 \times 10^{11} M_{\odot}$. Mrk 1216 is similar to NGC 1277 and NGC 1271 – the two compact, high-dispersion galaxies from the HET Massive Galaxy Survey that have prior stellar-dynamical M_{BH} measurements from AO observations. All three galaxies resemble the quiescent galaxies at $z \sim 2$ given their small but massive nature, their stellar mass surface density profiles, their strong rotation, and (in the cases of NGC 1277 and NGC 1271) their uniformly old stellar populations. Therefore, Mrk 1216, as well as NGC 1277 and NGC 1271, appear to be relics of the $z \sim 2$ red nuggets, and their black holes may imply that the normalization of the $M_{\text{BH}} - L_{\text{bul}}$ and $M_{\text{BH}} - M_{\text{bul}}$ relations were higher at earlier times. In other words, perhaps black hole growth precedes that of its host galaxy. Another possibility is that the galaxies are simply unusual and are in the tail of a distribution between M_{BH} and galaxy properties that still needs to be firmly established. Distinguishing between the two scenarios requires obtaining a more complete census of local black holes in a wide range of galaxies with diverse evolutionary histories.

Based on observations obtained at the Gemini Observatory acquired through the Gemini Science Archive and processed using the Gemini IRAF package, which is operated by the Association of Universities for Research in Astronomy, Inc., under a cooperative agreement with the NSF on behalf of the Gemini partnership: the National Science Foundation (United States), the National Research Council (Canada), CONICYT (Chile), the Australian Research Council (Australia), Ministério da Ciência, Tecnologia e Inovação (Brazil) and Ministe-

rio de Ciencia, Tecnología e Innovación Productiva (Argentina), under program GN-2013A-Q-1. Also based on observations made with the NASA/ESA Hubble Space Telescope, obtained at the Space Telescope Science Institute, which is operated by the Association of Universities for Research in Astronomy, Inc., under NASA contract NAS 5-26555. These observations are associated with program #13050. Based on observations collected at the Centro Astronómico Hispano Alemán (CAHA) at Calar Alto, operated jointly by the Max-Planck Institut für Astronomie and the Instituto de Astrofísica de Andalucía (CSIC). This work is further based on observations obtained with the Hobby-Eberly Telescope (HET). The HET is a joint project of the University of Texas at Austin, the Pennsylvania State University, Ludwig-Maximilians-Universität München, and Georg-August-Universität Göttingen. The HET is named in honor of its principal benefactors, William P. Hobby and Robert E. Eberly. This material is based in part upon work J. L. W. conducted as an NSF Astronomy and Astrophysics Postdoctoral Fellow under Award No. 1102845. The authors further acknowledge the Texas Advanced Computing Center (TACC; <http://www.tacc.utexas.edu>) at the University of Texas at Austin for providing HPC resources that have contributed to the research results reported within this paper. This research has made use of the NASA/IPAC Extragalactic Database which is operated by the Jet Propulsion Laboratory, California Institute of Technology, under contract with NASA. We acknowledge the usage of the HyperLeda database (<http://leda.univ-lyon1.fr>).

REFERENCES

- Alatalo, K., Davis, T. A., Bureau, M., et al. 2013, MNRAS, 432, 1796
 Barber, C., Schaye, J., Bower, R. G., et al. 2016, MNRAS, 460, 1147
 Barth, A. J., Darling, J., Boizelle, B. D., et al. 2016a, ApJ, 823, 51
 Barth, A. J., Boizelle, B. D., Darling, J., et al. 2016b, ApJ, 822, L28
 Beifiori, A., Courteau, S., Corsini, E. M., & Zhu, Y. 2012, MNRAS, 419, 2497

- Bender, R., Saglia, R. P., & Gerhard, O. E. 1994, *MNRAS*, 269, 785
- Binney, J., & Merrifield, M. 1998, *Galactic Astronomy*. Princeton Univ. Press, Princeton, NJ
- Boccas, M., Rigaut, F., Bec, M., et al. 2006, *Proc. SPIE*, 6272, 114
- Cappellari, M., & Copin, Y. 2003, *MNRAS*, 342, 345
- Cappellari, M., & Emsellem, E. 2004, *PASP*, 116, 138
- Crain, R. A., Schaye, J., Bower, R. G., et al. 2015, *MNRAS*, 450, 1937
- Cretton, N., & van den Bosch, F. C. 1999, *ApJ*, 514, 704
- de Francesco, G., Capetti, A., & Marconi, A. 2006, *A&A*, 460, 439
- Drehmer, D. A., Storch-Bergmann, T., Ferrari, F., Cappellari, M., & Riffel, R. A. 2015, *MNRAS*, 450, 128
- Emsellem, E., Monnet, G., & Bacon, R. 1994, *A&A*, 285, 723
- Emsellem, E. 2013, *MNRAS*, 433, 1862
- Fabian, A. C. 1999, *MNRAS*, 308, L39
- Falcón-Barroso, J., Sánchez-Blázquez, P., Vazdekis, A., et al. 2011, *A&A*, 532, 95
- Ferrarese, L., & Merritt, D. 2000, *ApJ*, 539, L9
- Ferré-Mateu, A., Mezcuá, M., Trujillo, I., Balcells, M., & van den Bosch, R. C. E. 2015, *ApJ*, 808, 79
- Fisher, D. 1997, *AJ*, 113, 950
- Gebhardt, K., Bender, R., Bower, G., et al. 2000, *ApJL*, 539, L13
- Gebhardt, K., & Thomas, J. 2009, *ApJ*, 700, 1690
- Gebhardt, K., Adams, J., Richstone, D., et al. 2011, *ApJ*, 729, 119
- Gonzaga, S., Hack, W., Fruchter, A., & Mack, J. 2012, *The DrizzlePac Handbook* (Baltimore, STScI)
- Graham, A. W., Durreé, M., Savorgnan, G. A. D., et al. 2016a, *ApJ*, 819, 43
- Graham, A. W., Ciambur, B. C., & Savorgnan, G. A. D. 2016b, accepted by *ApJ*, arXiv:1608.00711
- Greene, J. E., Peng, C. Y., Kim, M., et al. 2010, *ApJ*, 721, 26
- Greene, J. E., Seth, A., Kim, M., et al. 2016, *ApJ*, 826, L32
- Gültekin, K., Richstone, D. O., Gebhardt, K., et al. 2009, *ApJ*, 698, 198
- Häring, N., & Rix, H.-W. 2004, *ApJ*, 604, L89
- Herriot, G., Morris, S., Anthony, A., et al. 2000, *Proc. SPIE*, 4007, 115
- Hill, G. J., Nicklas, H. E., MacQueen, P. J., et al. 1998, *Proc. SPIE*, 3355, 375
- Ho, L. C., Sarzi, M., Rix, H.-W., et al. 2002, *PASP*, 114, 137
- Husemann, B., Jahnke, K., Sánchez, S. F., et al. 2013, *A&A*, 549, 87
- Jahnke, K., & Macciò, A. V. 2011, *ApJ*, 734, 92
- Kelz, A., Verheijen, M. A. W., Roth, M. M., et al. 2006, *PASP*, 118, 129
- Kormendy, J., & Richstone, D. 1995, *ARA&A*, 33, 581
- Kormendy, J., & Ho, L. C. 2013, *ARA&A*, 51, 511
- Krajnović, D., Cappellari, M., Emsellem, E., McDermid, R. M., & de Zeeuw, P. T. 2005, *MNRAS*, 357, 1113
- Krajnović, D., McDermid, R. M., Cappellari, M., & Davies, R. L. 2009, *MNRAS*, 399, 1839
- Krist, J., & Hook, R. 2004, *The Tiny Tim User's Guide* (Baltimore:STScI)
- Lauer, T. R., Faber, S. M., Richstone, D., et al. 2007a, *ApJ*, 662, 808
- Lauer, T. R., Tremaine, S., Richstone, D., & Faber, S. M. 2007b, *ApJ*, 670, 249
- Läsker, R., Ferrarese, L., van de Ven, G., & Shankar, F. 2014, *ApJ*, 780, 70
- Läsker, R., Greene, J. E., Seth, A., et al. 2016, *ApJ*, 825, 3
- Marconi, A., & Hunt, L. K. 2003, *ApJ*, 589, L21
- Marconi, A., Risaliti, G., Gilli, R., et al. 2004, *MNRAS*, 351, 169
- Martín-Navarro, I., La Barbera, F., Vazdekis, A., et al. 2015, *MNRAS*, 451, 1081
- McConnell, N. J., Ma, C.-P., Murphy, J. D., et al. 2012, *ApJ*, 756, 179
- McConnell, N. J., & Ma, C.-P. 2013, *ApJ*, 764, 184
- McConnell, N. J., Chen, S.-F. S., Ma, C.-P., et al. 2013, *ApJ*, 768, 21
- McGregor, P. J., Hart, J., Conroy, P. G., et al. 2003, *Proc. SPIE*, 4841, 1581
- Monnet, G., Bacon, R., & Emsellem, E. 1992, *A&A*, 253, 366
- Mould, J. R., Huchra, J. P., Freedman, W. L., et al. 2000, *ApJ*, 529, 786
- Navarro, J. F., Frenk, C. S., & White, S. D. M. 1996, *ApJ*, 462, 563
- Onken, C. A., Valluri, M., Brown, J. S., et al. 2014, *ApJ*, 791, 37
- Peng, C. Y. 2007, *ApJ*, 671, 1098
- Peng, C. Y., Ho, L. C., Impey, C. D., & Rix, H.-W. 2010, *AJ*, 139, 2097
- Robertson, B., Hernquist, L., Cox, T. J., et al. 2006, *ApJ*, 641, 90
- Roth, M. M., Kelz, A., Fechner, T., et al. 2005, *PASP*, 117, 620
- Rusli, S. P., Thomas, J., Erwin, P., et al. 2011, *MNRAS*, 410, 1223
- Rusli, S. P., Thomas, J., Saglia, R. P., et al. 2013, *AJ*, 146, 45
- Saglia, R. P., Opitsch, M., Erwin, P., et al. 2016, *ApJ*, 818, 47
- Sánchez, S. F., Kennicutt, R. C., Gil de Paz, A., et al. 2012, *A&A*, 538, 8
- Sánchez-Blázquez, P., Peletier, R. F., Jiménez-Vicente, J., et al. 2006, *MNRAS*, 371, 703
- Sani, E., Marconi, A., Hunt, L. K., & Risaliti, G. 2011, *MNRAS*, 413, 1479
- Savorgnan, G. A. D., Graham, A. W., Marconi, A., & Sani, E. 2016, *ApJ*, 817, 21
- Savorgnan, G. A. D., & Graham, A. W. 2016, *MNRAS*, 457, 320
- Scharwächter, J., Combes, F., Salomé, P., Sun, M., & Krips, M. 2016, *MNRAS*, 457, 4272
- Schaye, J., Crain, R. A., Bower, R. G., et al. 2015, *MNRAS*, 446, 521
- Schulze, A., & Gebhardt, K. 2011, *ApJ*, 729, 21
- Schlafly, E. F., & Finkbeiner, D. P. 2011, *ApJ*, 737, 103
- Seth, A. C., van den Bosch, R., Mieske, S., et al. 2014, *Natur*, 513, 398
- Shankar, F., Weinberg, D. H., & Miralda-Escudé, J. 2009, *ApJ*, 690, 20
- Shapiro, K. L., Cappellari, M., de Zeeuw, T., et al. 2006, *MNRAS*, 370, 559
- Silk, J., & Rees, M. J. 1998, *A&A*, 331, L1
- Skrutskie, M. F., Cutri, R. M., Stiening, R., et al. 2006, *AJ*, 131, 1163
- Thomas, J., Ma, C.-P., McConnell, N. J., et al. 2016, *Natur*, 532, 340
- Trujillo, I., Cenarro, A. J., de Lorenzo-Cáceres, A., et al. 2009, *ApJL*, 692, L118
- Trujillo, I., Ferré-Mateu, A., Balcells, M., Vazdekis, A., & Sánchez-Blázquez, P. 2014, *ApJL*, 780, L20
- Valdes, F., Gupta, R., Rose, J. A., Singh, H. P., & Bell, D. J. 2004, *ApJS*, 152, 251
- van den Bosch, R. C. E., van de Ven, G., Verolme, E. K., Cappellari, M., & de Zeeuw, P. T. 2008, *MNRAS*, 385, 647
- van den Bosch, R. C. E., & van de Ven, G. 2009, *MNRAS*, 398, 1117
- van den Bosch, R. C. E., & de Zeeuw, P. T. 2010, *MNRAS*, 401, 1770
- van den Bosch, R. C. E., Gebhardt, K., Gültekin, K., et al. 2012, *Nature*, 491, 729
- van den Bosch, R. C. E., Gebhardt, K., Gültekin, K., Yıldırım, A., & Walsh, J. L. 2015, *ApJS*, 218, 10
- van den Bosch, R. C. E. 2016, *ApJ*, 831, 134
- van der Marel, R. P., & Franx, M. 1993, *ApJ*, 407, 525
- van der Wel, A., Rix, H.-W., Wuyts, S., et al. 2011, *ApJ*, 730, 38
- van der Wel, A., Bell, E. F., Häussler, B., et al. 2012, *ApJS*, 203, 24
- van Dokkum, P. G., Whitaker, K. E., Brammer, G., et al. 2010, *ApJ*, 709, 1018
- Vazdekis, A., Casuso, E., Peletier, R. F., & Beckman, J. E. 1996, *ApJS*, 106, 307
- Verheijen, M. A. W., Bershady, M. A., Andersen, D. R., et al. 2004, *AN*, 325, 151
- Walsh, J. L., van den Bosch, R. C. E., Barth, A. J., & Sarzi, M. 2012, *ApJ*, 753, 79
- Walsh, J. L., Barth, A. J., Ho, L. C., & Sarzi, M. 2013, *ApJ*, 770, 86
- Walsh, J. L., van den Bosch, R. C. E., Gebhardt, K., et al. 2015, *ApJ*, 808, 183
- Walsh, J. L., van den Bosch, R. C. E., Gebhardt, K., et al. 2016, *ApJ*, 817, 2
- Wellons, S., Torrey, P., Ma, C.-P., et al. 2016, *MNRAS*, 456, 1030
- Winge, C., Riffel, R. A., & Storch-Bergmann, T. 2009, *ApJS*, 185, 186

- Yildirim, A., van den Bosch, R. C. E., van de Ven, G., et al. 2015, MNRAS, 452, 1792
- Yildirim, A., van den Bosch, R. C. E., van de Ven, G., et al. 2016a, MNRAS, 456, 538